

Received March 24, 2021, accepted April 9, 2021, date of publication April 13, 2021, date of current version April 20, 2021.

Digital Object Identifier 10.1109/ACCESS.2021.3072918

Design and Analysis of a Novel Dual-Airgap Dual Permanent Magnet Vernier Machine

MINGYUAN JIANG¹, WEINONG FU¹, AND SHUANGXIA NIU¹, (Senior Member, IEEE)

Department of Electrical Engineering, The Hong Kong Polytechnic University, Hong Kong

Corresponding author: Weinong Fu (eewnfu@polyu.edu.hk)

This work was supported by the Hong Kong Research Grants Council, Hong Kong, under Project PolyU 152143/18E and Project PolyU 152058/17E.

ABSTRACT A novel dual-airgap permanent magnet Vernier machine (DADPMVM) is proposed and analyzed in this paper. The key of this design is combining the double-concentric-rotor structure, the dual permanent magnet structure along with the Vernier structure to improve the torque density while remaining the motor's volume unchanged. The maximized use of the winding length and the reduction of copper loss are also the main merits of this design. The machine structure and operating principle are discussed, and its transient performance is analyzed by using the finite element method (FEM). Two different configurations of pole pairs and two different structures are designed in the same peripheral dimension configuration and compared with the proposed machine by FEM. The results of the comparison are used to confirm the outstanding performance of the proposed machine. The torque density per machine volume can exceed 100 kNm/m^3 with the proper cooling method.

INDEX TERMS Dual airgap, dual permanent magnet, Vernier machine, high torque density.

I. INTRODUCTION

The demand of high torque, low speed electric machines for applications such as electric vehicle propulsion and wind power generation are increasing rapidly nowadays. Conventionally, machines operating in low speed tend to have large volume, large pole-pair number and large slot number, which are unsuitable for certain circumstances.

A lot of studies have been made to reduce the volume and improve the torque density. The Permanent Magnet Vernier Machine (PMVM) is one of the prospective choices for high torque applications [1]–[5]. With the magnetic gearing effect, a small movement of rotor makes a large change in the flux, which results the high torque [6]–[8]. Specific space harmonics can be produced in the air gap with a relative small number of pole pairs and slots by using the magnetic gearing effect. Consequently, the volume can be reduced.

There are a number of topologies for PMVM, as the placement of the PM sources can be on either side or both sides of stator and rotor [9], [10]. The most attractive topology is the dual PM Vernier machine (DPMVM), which embedded the PM sources on both sides of stator and rotor [11]–[13]. With dual PM sources working simultaneously, this structure has relative high torque density.

The associate editor coordinating the review of this manuscript and approving it for publication was Montserrat Rivas.

In order to further improve the torque density within the limited machine volume, structures like dual-excitation, dual-airgap and multi-excitation-multi-airgap have been studied [14]. The dual-airgap (DA) structure with the utilization of drum winding, i.e. coils wound around the stator yoke is the most attractive structure [15], [16]. On the one hand, one set of drum winding can be used for excitation for both inner rotor and outer rotor, which maximizes the use of the winding for radial flux motor. On the other hand, the end of winding can be designed to be much shorter, especially when comparing to windings with large coil pitch. Therefore, the copper loss can be greatly reduced.

In this paper, the proposed DADPMVM will be analyzed. In Section II, the machine structure and the operating principle will be introduced. The finite element analysis (FEM) analysis of DADPMVM, the comparison with two other pole-pair configuration and the comparison with two different structures will be presented in Section III. The conclusions are drawn in Section IV.

II. MACHINE STRUCTURE AND OPERATING PRINCIPLE

A. MACHINE STRUCTURE

Fig. 1 shows the structure of proposed DADPMVM in this paper. This machine consists of a 24-slot-on-both-side

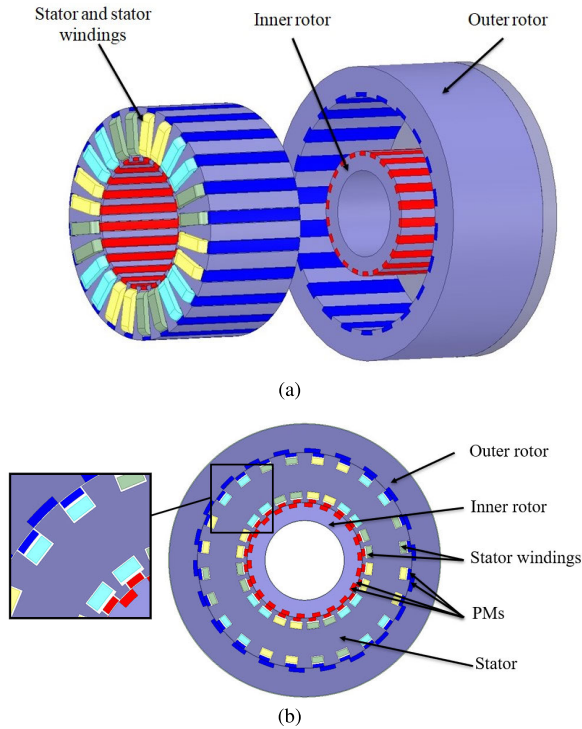


FIGURE 1. Machine configuration of DADPMVM. (a) Machine structure. (b) Cross Section.

stator, a 22-pole-pair inner rotor and a 22-pole-pair outer rotor. The stator is placed between two concentric rotors. A 2-pole-pair, three phase drum winding is placed in the stator slots.

Four sets of PMs are placed at inner rotor, outer rotor and both sides of the stator. The inner-side stator PMs and the inner rotor PMs (red parts in Fig. 1(b)) are both in radial positive magnetization direction, i.e. outwards; the outer-side stator PMs and the outer rotor PMs (blue parts in Fig. 1(b)) are both in radial negative magnetization direction, i.e. inwards. This configuration of PMs enables the magnetic flux to concentrate into the stator yoke. In order to reduce over saturation in the yoke, the stator yoke length should be relatively long.

Both sides of the stator PMs are mounted on the slot openings and both sides of the rotor PMs are equipped in the rotor slots. With the modulation of rotor core teeth and the interaction with the armature windings, the stator PMs form pole pair with their adjacent stator core teeth. Similarly, the rotor PMs form pole pair with their adjacent rotor core teeth by modulating with the stator core teeth and interacting with the armature windings as well. High torque density is contributed by dual PM sources' synchronous torque generation.

B. OPERATING PRINCIPLE

In this proposed machine, suppose the pole pair number of the stator PMs, rotor PMs and winding is Z_s , Z_r and p_a .

1) PERMEANCE

The permeance per unit area of the airgap can be expressed as

$$\Lambda = \frac{B}{F} \tag{1}$$

where B is the flux density in airgap and F is the magnetic motive force (mmf). When there are no slots on both sides of the airgap, the permeance of the airgap per unit area Λ_0 can be expressed as

$$\Lambda_0 = \frac{\mu_0}{\delta} \tag{2}$$

where μ_0 is the permeance of the air and δ is the length of airgap. Because the proposed machine has slots on both sides of the airgaps, for the convenience of analyzing, the relative permeance λ is often used. The relationship between λ and Λ can be given as

$$\lambda = \frac{\Lambda}{\Lambda_0} \tag{3}$$

The relative permeance of stator teeth and rotor teeth along the airgap are periodic functions of space angle θ . By the Fourier decomposition, they can be expressed as

$$\lambda_s = \lambda_{s0} + \sum_{\alpha=1,2,3\dots} \lambda_{sm\alpha} \cos[\alpha Z_s(\theta + \phi_{\lambda_s})] \tag{4}$$

$$\lambda_r = \lambda_{r0} + \sum_{\beta=1,2,3\dots} \lambda_{rm\beta} \cos[\beta Z_r(\theta + \phi_{\lambda_r}) - \beta Z_r \Omega t] \tag{5}$$

where αZ_s and βZ_r are the order (i.e. pole-pair number) of the stator and rotor harmonic component, λ_{s0} and λ_{r0} are the average value of stator teeth relative permeance and rotor teeth relative permeance, $\lambda_{sm\alpha}$ is the magnitude of αZ_s -th order stator teeth relative permeance component, $\lambda_{rm\beta}$ is the magnitude of βZ_r -th order rotor teeth relative permeance component, Ω is the mechanical angular speed and ϕ_{λ_s} , ϕ_{λ_r} are the initial phase angles, respectively. Because the high-order components' magnitude is much smaller than the fundamental component, by keeping the fundamental component and neglecting the high-order components (i.e. $\alpha = 1, \beta = 1$), (4) and (5) can be simplified as

$$\lambda_s = \lambda_{s0} + \lambda_{sm} \cos[Z_s(\theta + \phi_{\lambda_s})] \tag{6}$$

$$\lambda_r = \lambda_{r0} + \lambda_{rm} \cos[Z_r(\theta + \phi_{\lambda_r}) - Z_r \Omega t] \tag{7}$$

where λ_{sm} , λ_{rm} are the magnitude of stator teeth and rotor teeth fundamental relative permeance components.

Therefore, the overall relative permeance of the airgap λ_g can be expressed as the product of the relative permeance of stator teeth and rotor teeth. From (3), (6), (7) and the mathematical identity of product to sum, i.e.

$$\cos(x) \cos(y) = \frac{1}{2} \cos(x + y) + \frac{1}{2} \cos(x - y)$$

the permeance of airgap can be expressed as

$$\begin{aligned} \Lambda_g &= \Lambda_0 \lambda_g \\ &= \Lambda_0 \lambda_s \lambda_r \\ &= \Lambda_0 \{ \lambda_{s0} + \lambda_{sm} \cos[Z_s(\theta + \phi_{\lambda_s})] \} \\ &\quad \times \{ \lambda_{r0} + \lambda_{rm} \cos[Z_r(\theta + \phi_{\lambda_r}) - \beta Z_r \Omega t] \} \\ &= \Lambda_{g0} + \Lambda_{g1} + \Lambda_{g2} + (\Lambda_{g3} + \Lambda_{g4}) \end{aligned} \quad (8)$$

where

$$\Lambda_{g0} = \Lambda_0 \lambda_{s0} \lambda_{r0} \quad (9)$$

$$\Lambda_{g1} = \Lambda_0 \lambda_{sm} \lambda_{r0} \cos(Z_s \theta + Z_s \phi_{\lambda_s}) \quad (10)$$

$$\Lambda_{g2} = \Lambda_0 \lambda_{rm} \lambda_{s0} \cos[Z_r(\theta - \Omega t) + Z_r \phi_{\lambda_r}] \quad (11)$$

$$\begin{aligned} \Lambda_{g3} &= \frac{1}{2} \Lambda_0 \lambda_{sm} \lambda_{rm} \cos \left[(Z_s + Z_r) \left(\theta - \frac{Z_r \Omega}{Z_s + Z_r} t \right) \right. \\ &\quad \left. + (Z_s \phi_{\lambda_s} + Z_r \phi_{\lambda_r}) \right] \end{aligned} \quad (12)$$

$$\begin{aligned} \Lambda_{g4} &= \frac{1}{2} \Lambda_0 \lambda_{sm} \lambda_{rm} \cos \left[(Z_s - Z_r) \left(\theta + \frac{Z_r \Omega}{Z_s - Z_r} t \right) \right. \\ &\quad \left. + (Z_s \phi_{\lambda_s} - Z_r \phi_{\lambda_r}) \right] \end{aligned} \quad (13)$$

2) MAGNETIC MOTIVE FORCE

The mmf produced by the stator PMs and rotor PMs can be expressed as

$$F_s = F_{s0} + F_{s1} \quad (14)$$

$$F_r = F_{r0} + F_{r1} \quad (15)$$

where

$$F_{s1} = F_{sm} \cos [Z_s(\theta + \phi_{F_s})] \quad (16)$$

$$F_{r1} = F_{rm} \cos [Z_r(\theta + \phi_{F_r}) - Z_r \Omega t] \quad (17)$$

In (14) - (17), F_{s0} and F_{r0} are the average value of stator PMs' mmf and rotor PMs' mmf, F_{s1} and F_{r1} are the fundamental component of stator PMs' mmf and rotor PMs' mmf, F_{sm} and F_{rm} are the magnitude of stator PMs' mmf fundamental component and rotor PMs' mmf fundamental component, ϕ_{F_s} and ϕ_{F_r} are the initial phase angle, respectively. F_{s0} and F_{r0} exist because all the PMs along the same airgap have the same magnetization direction.

The total mmf of the armature winding can be expressed as

$$F_a = F_{am} \cos [p_a(\theta + \phi_a) + k_{da} \omega_a t] \quad (18)$$

where F_{am} is the magnitude of the armature winding's mmf, ω_a is the angular frequency of armature winding input current and ϕ_a is the initial phase angle. k_{da} is the direction coefficient of excited mmf. When $k_{da} = -1$, it indicates the magnetic field excited by armature winding rotates in positive direction (i.e. same as the mechanical rotating direction). When $k_{da} = +1$, it indicates the magnetic field excited by armature winding rotates in negative direction (i.e. opposite with the mechanical rotating direction).

3) FLUX DENSITY

Based on (1), each component of the magnetic flux density b_n in the airgap can be expressed as

$$B_n = F_n \Lambda_n = B_{nm} \cos [p(\theta + k_{dn} \omega t) + \phi] \quad (19)$$

where F_n and Λ_n are the mmf components and the permeance components, B_{nm} is the magnitude of the magnetic flux density components, p is the pole-pair number of the magnetic flux density, ω is the angular speed of flux density and ϕ is the initial phase angle. k_{dn} is the direction coefficient of magnetic flux density, which has the same setting as k_{da} (i.e. positive direction when $k_{dn} = -1$, negative direction when $k_{dn} = +1$ and stationary when $k_{dn} = 0$).

From (9) - (13), (14) and (16), the flux density produced by the modulation of stator PMs and permeance of airgap is

$$\begin{aligned} B_s &= F_s \Lambda_g \\ &= B_{s00} + B_{s01} + B_{s02} + B_{s03} + B_{s04} \\ &\quad + B_{s10} + B_{s11} + B_{s12} + B_{s13} + B_{s14} \end{aligned} \quad (20)$$

where

$$B_{s00} = F_{s0} \Lambda_{g0} = F_{s0} \Lambda_0 \lambda_{s0} \lambda_{r0} \quad (21)$$

$$\begin{aligned} B_{s01} &= F_{s0} \Lambda_{g1} \\ &= F_{s0} \Lambda_0 \lambda_{sm} \lambda_{r0} \cos(Z_s \theta + Z_s \phi_{\lambda_s}) \end{aligned} \quad (22)$$

$$\begin{aligned} B_{s02} &= F_{s0} \Lambda_{g2} \\ &= F_{s0} \Lambda_0 \lambda_{rm} \lambda_{s0} \cos[Z_r(\theta - \Omega t) + Z_r \phi_{\lambda_r}] \end{aligned} \quad (23)$$

$$\begin{aligned} B_{s03} &= F_{s0} \Lambda_{g3} \\ &= \frac{1}{2} F_{s0} \Lambda_0 \lambda_{sm} \lambda_{rm} \cos \left[(Z_s + Z_r) \left(\theta - \frac{Z_r \Omega}{Z_s + Z_r} t \right) \right. \\ &\quad \left. + (Z_s \phi_{\lambda_s} + Z_r \phi_{\lambda_r}) \right] \end{aligned} \quad (24)$$

$$\begin{aligned} B_{s04} &= F_{s0} \Lambda_{g4} \\ &= \frac{1}{2} F_{s0} \Lambda_0 \lambda_{sm} \lambda_{rm} \cos \left[(Z_s - Z_r) \left(\theta + \frac{Z_r \Omega}{Z_s - Z_r} t \right) \right. \\ &\quad \left. + (Z_s \phi_{\lambda_s} - Z_r \phi_{\lambda_r}) \right] \end{aligned} \quad (25)$$

$$\begin{aligned} B_{s10} &= F_{s1} \Lambda_{g0} \\ &= F_{sm} \Lambda_0 \lambda_{s0} \lambda_{r0} \cos(Z_s \theta + Z_s \phi_{\lambda_s}) \end{aligned} \quad (26)$$

$$B_{s11} = F_{s1} \Lambda_{g1} = B_{s111} + B_{s112} \quad (27)$$

$$B_{s12} = F_{s1} \Lambda_{g2} = B_{s121} + B_{s122} \quad (28)$$

$$B_{s13} = F_{s1} \Lambda_{g3} = B_{s131} + B_{s132} \quad (29)$$

$$B_{s14} = F_{s1} \Lambda_{g4} = B_{s141} + B_{s142} \quad (30)$$

where (27) - (30) can be further decomposed as

$$B_{s111} = \frac{1}{2} F_{sm} \Lambda_0 \lambda_{sm} \lambda_{r0} \cos(2Z_s \theta + 2Z_s \phi_{\lambda_s}) \quad (31)$$

$$B_{s112} = \frac{1}{2} F_{sm} \Lambda_0 \lambda_{sm} \lambda_{r0} \quad (32)$$

$$\begin{aligned} B_{s121} &= \frac{1}{2} F_{sm} \Lambda_0 \lambda_{rm} \lambda_{s0} \cos \left[(Z_s + Z_r) \left(\theta - \frac{Z_r \Omega}{Z_s + Z_r} t \right) \right. \\ &\quad \left. + (Z_s \phi_{\lambda_s} + Z_r \phi_{\lambda_r}) \right] \end{aligned} \quad (33)$$

$$\begin{aligned} B_{s122} &= \frac{1}{2} F_{sm} \Lambda_0 \lambda_{rm} \lambda_{s0} \cos \left[(Z_s - Z_r) \left(\theta + \frac{Z_r \Omega}{Z_s - Z_r} t \right) \right. \\ &\quad \left. + (Z_s \phi_{\lambda_s} - Z_r \phi_{\lambda_r}) \right] \end{aligned} \quad (34)$$

$$\begin{aligned} B_{s131} &= \frac{1}{4} F_{sm} \Lambda_0 \lambda_{sm} \lambda_{rm} \cos \left[(2Z_s + Z_r) \left(\theta - \frac{Z_r \Omega}{2Z_s + Z_r} t \right) \right. \\ &\quad \left. + (2Z_s \phi_{\lambda_s} + Z_r \phi_{\lambda_r}) \right] \end{aligned} \quad (35)$$

$$B_{s132} = \frac{1}{4} F_{sm} \Lambda_0 \lambda_{sm} \lambda_{rm} \cos [Z_r(\theta - \Omega t) + Z_r \phi_{\lambda_r}] \quad (36)$$

$$B_{s141} = \frac{1}{4} F_{sm} \Lambda_0 \lambda_{sm} \lambda_{rm} \cos[(2Z_s - Z_r)(\theta + \frac{Z_r \Omega}{2Z_s - Z_r} t) + (2Z_s \phi_{\lambda s} - Z_r \phi_{\lambda r})] \quad (37)$$

$$B_{s142} = \frac{1}{4} F_{sm} \Lambda_0 \lambda_{sm} \lambda_{rm} \cos[Z_r(\theta - \Omega t) + Z_r \phi_{\lambda r}] \quad (38)$$

Because the number of equations for magnetic flux density components is large, for the convenience of further analysis, the coefficients of (21) - (38) is sorted and listed in Table 1 based on (19).

TABLE 1. Coefficients of magnetic flux components excited by stator PMs.

B_n	F_n	Λ_n	p	ω	k_{dn}
B_{s00}	F_{s0}	Λ_{g0}	0	0	0
B_{s01}	F_{s0}	Λ_{g1}	Z_s	0	0
B_{s02}	F_{s0}	Λ_{g2}	Z_r	Ω	-1
B_{s03}	F_{s0}	Λ_{g3}	$(Z_s + Z_r)$	$\frac{Z_r \Omega}{Z_s + Z_r}$	-1
B_{s04}	F_{s0}	Λ_{g4}	$(Z_s - Z_r)$	$\frac{Z_r \Omega}{Z_s - Z_r}$	+1
B_{s10}	F_{s1}	Λ_{g0}	Z_s	0	0
B_{s111}	F_{s1}	Λ_{g1}	$2Z_s$	0	0
B_{s112}	F_{s1}	Λ_{g1}	0	0	0
B_{s121}	F_{s1}	Λ_{g2}	$(Z_s + Z_r)$	$\frac{Z_r \Omega}{Z_s + Z_r}$	-1
B_{s122}	F_{s1}	Λ_{g2}	$(Z_s - Z_r)$	$\frac{Z_r \Omega}{Z_s - Z_r}$	+1
B_{s131}	F_{s1}	Λ_{g3}	$(2Z_s + Z_r)$	$\frac{Z_r \Omega}{2Z_s + Z_r}$	-1
B_{s132}	F_{s1}	Λ_{g3}	Z_r	Ω	-1
B_{s141}	F_{s1}	Λ_{g4}	$(2Z_s - Z_r)$	$\frac{Z_r \Omega}{2Z_s - Z_r}$	+1
B_{s142}	F_{s1}	Λ_{g4}	Z_r	Ω	-1

With the similar process, the coefficients of magnetic flux density components excited by rotor PMs and armature winding current after calculation are listed in Table 2 and Table 3. For the simplified form of ω , in Table 3, all k_{da} are put in the numerator because it has the feature of $k_{da} \cdot k_{da} = 1$.

TABLE 2. Coefficients of magnetic flux components excited by rotor PMs.

B_n	F_n	Λ_n	p	ω	k_{dn}
B_{r00}	F_{r0}	Λ_{g0}	0	0	0
B_{r01}	F_{r0}	Λ_{g1}	Z_s	0	0
B_{r02}	F_{r0}	Λ_{g2}	Z_r	Ω	-1
B_{r03}	F_{r0}	Λ_{g3}	$(Z_s + Z_r)$	$\frac{Z_r \Omega}{Z_s + Z_r}$	-1
B_{r04}	F_{r0}	Λ_{g4}	$(Z_s - Z_r)$	$\frac{Z_r \Omega}{Z_s - Z_r}$	+1
B_{r10}	F_{r1}	Λ_{g0}	Z_r	Ω	-1
B_{r111}	F_{r1}	Λ_{g1}	$(Z_s + Z_r)$	$\frac{Z_r \Omega}{Z_s + Z_r}$	-1
B_{r112}	F_{r1}	Λ_{g1}	$(Z_s - Z_r)$	$\frac{Z_r \Omega}{Z_s - Z_r}$	+1
B_{r121}	F_{r1}	Λ_{g2}	$2Z_r$	Ω	-1
B_{r122}	F_{r1}	Λ_{g2}	0	0	0
B_{r131}	F_{r1}	Λ_{g3}	$(2Z_r + Z_s)$	$\frac{Z_r \Omega}{2Z_r + Z_s}$	-1
B_{r132}	F_{r1}	Λ_{g3}	Z_s	0	0
B_{r141}	F_{r1}	Λ_{g4}	Z_s	0	0
B_{r142}	F_{r1}	Λ_{g4}	$(2Z_r - Z_s)$	$\frac{Z_r \Omega}{2Z_r - Z_s}$	-1

4) GENERAL PRINCIPLE

For the magnetic flux density components excited by stator PMs, rotor PMs and armature winding, synchronous torque

TABLE 3. Coefficients of magnetic flux components excited by armature winding current.

B_n	F_n	Λ_n	p	ω	k_{dn}
B_{a0}	F_a	Λ_{g0}	p_a	$\frac{\omega_a}{p_a}$	$+k_{da}$
B_{a11}	F_a	Λ_{g1}	$(Z_s + p_a)$	$\frac{\omega_a}{Z_s + p_a}$	$+k_{da}$
B_{a12}	F_a	Λ_{g1}	$(Z_s - p_a)$	$\frac{\omega_a}{Z_s - p_a}$	$-k_{da}$
B_{a21}	F_a	Λ_{g2}	$(Z_r + p_a)$	$\frac{\omega - k_{da} Z_r \Omega}{Z_r + p_a}$	$+k_{da}$
B_{a22}	F_a	Λ_{g2}	$(Z_r - p_a)$	$\frac{\omega + k_{da} Z_r \Omega}{Z_r - p_a}$	$-k_{da}$
B_{a31}	F_a	Λ_{g3}	$(Z_s + Z_r + p_a)$	$\frac{\omega - k_{da} Z_r \Omega}{Z_s + Z_r + p_a}$	$+k_{da}$
B_{a32}	F_a	Λ_{g3}	$(Z_s + Z_r - p_a)$	$\frac{\omega + k_{da} Z_r \Omega}{Z_s + Z_r - p_a}$	$-k_{da}$
B_{a41}	F_a	Λ_{g4}	$(Z_s - Z_r + p_a)$	$\frac{\omega + k_{da} Z_r \Omega}{Z_s - Z_r + p_a}$	$+k_{da}$
B_{a42}	F_a	Λ_{g4}	$(Z_s - Z_r - p_a)$	$\frac{\omega - k_{da} Z_r \Omega}{Z_s - Z_r - p_a}$	$-k_{da}$

can only be generated when their pole-pair number, angular speed and rotating direction are the same.

Based on this principle, when $Z_s > Z_r$, the relationship can be concluded as

$$\begin{cases} p = p_a = Z_s - Z_r \\ \omega = \frac{\omega_a}{p_a} = \frac{Z_r}{Z_s - Z_r} \Omega \\ k_{dn} = +1 \end{cases} \quad (39)$$

Under the circumstances of (39),

- 1) For B_{s04} and B_{s122} from Table 1, B_{r04} and B_{r122} from Table 2, and B_{a0} from Table 3, they are all $(Z_s - Z_r)$ -th components of magnetic flux density with the angular speed of $(Z_r/p_a)\Omega$ rotating in negative direction.
- 2) For B_{s02} , B_{s132} and B_{s142} from Table 1, B_{r02} and B_{r10} from Table 2, and B_{a12} from Table 3, they are all Z_r -th components of magnetic flux density with the angular speed of Ω rotating in positive direction.
- 3) For B_{s01} and B_{s10} from Table 1, B_{r01} , B_{r132} and B_{r141} from Table 2, and B_{a21} from Table 3, they are all Z_s -th components of magnetic flux density with no angular speed.

The $(Z_s - Z_r)$ -th, Z_r -th and Z_s -th component are the effective magnetic flux density components which generate synchronous torque.

When $Z_s < Z_r$:

$$\begin{cases} p = p_a = Z_r - Z_s \\ \omega = \frac{\omega_a}{p_a} = \frac{Z_r}{Z_r - Z_s} \Omega \\ k_{dn} = -1 \end{cases} \quad (40)$$

Under the circumstances of (40),

- 1) For B_{s04} and B_{s122} from Table 1, B_{r04} and B_{r122} from Table 2, and B_{a0} from Table 3, they are all $(Z_r - Z_s)$ -th components of magnetic flux density with the angular speed of $(Z_r/p_a)\Omega$ rotating in positive direction.
- 2) For B_{s01} and B_{s10} from Table 1, B_{r01} , B_{r132} and B_{r141} from Table 2, and B_{a22} from Table 3, they are all Z_s -th

components of magnetic flux density with no angular speed.

- 3) For B_{s02} , B_{s132} and B_{s142} from Table 1, B_{r02} and B_{r10} from Table 2, and B_{a11} from Table 3, they are all Z_r -th components of magnetic flux density with the angular speed of Ω rotating in positive direction.

The $(Z_r - Z_s)$ -th, Z_s -th and Z_r -th component are the effective magnetic flux density components which generate synchronous torque.

There is also another relationship rarely used, which is

$$\begin{cases} p = p_a = Z_s + Z_r \\ \omega = \frac{\omega_a}{p_a} = \frac{Z_r}{Z_s + Z_r} \Omega \\ k_{dn} = -1 \end{cases} \quad (41)$$

This is because its gear ratio is small. The gear ratio can be expressed as

$$G = \frac{\omega}{\Omega} = \frac{Z_r}{p_a} \quad (42)$$

Usually higher torque can be transmitted when gear ratio is higher. In the proposed machine, the gear ratio of (41) is obviously much lower than (39) and (40). In order to get higher torque density, the machine proposed in this paper chooses the relationship of (39).

From the equation of p in (39) and (40), when the pole-pair number of PMs and the number of modulation segments is close, the pole-pair number of the armature winding as well as the magnetic field is small. The action of alignment and misalignment is very similar to the characteristics of vernier gauge, which is the origin of this type of machine's name. From the equation of ω in (39) and (40), it can be observed that the angular speed of the magnetic field excited by armature winding is G times higher than the mechanical rotating speed, which is because that the flux linkage reverses polarity when the rotor rotates just one PM pole pitch. This makes the changing rate of the flux linkage high, which directly results the Electric Motive Force (EMF) to have high frequency and magnitude. This phenomenon is also called magnetic gear effect [6], which allow the machine to have the feature of relatively low-speed and high-torque feature.

Consequently, the parameters in this paper are $p_a = 2$, $Z_s = 24$, $Z_r = 22$.

III. ANALYSIS

The proposed DADPMVM has two air gaps, two rotating parts and there are PM sources on both sides, which make it hard to analyze by the magnetic circuit method alone. With the help of FEM computing software ANSYS Maxwell, an FEM model is built for the proposed machine in order to do the further analysis. The design is based on in-wheel drive specification. The basic design parameters are listed in Table 4.

TABLE 4. The basic parameters of DADPMVM.

Parameter	Value
Rated speed	985 rpm
Rated Current (rms)	110 A
Rated DC-link voltage	240 V
Rated Torque	430 Nm
Frequency	361 Hz
Outer diameter	340 mm
Core length	130 mm
Air gap length	0.5 mm
Thickness of stator PMs	4 mm
Thickness of rotor PMs	5 mm
Material of PM	NdFe35

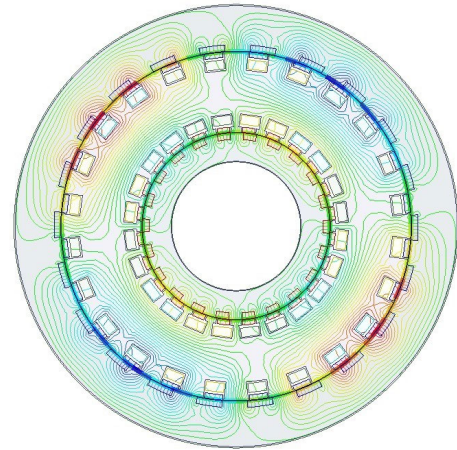


FIGURE 2. The magnetic flux line at no load.

A. NO-LOAD ANALYSIS

Based on the parameters in Table 4, the magnetic flux line distribution at no-load condition is calculated and the result is shown in Fig. 2. The modulated 2-pole-pair magnetic field can be clearly observed in the stator yoke and both rotors' yoke. The majority of the flux is flowing from inner rotor yoke and outer rotor yoke into the stator yoke. From Fig. 2, it can be shown that most of the flux is able to pass through the air gap for torque transmission and power conversion.

The flux density waveform of the inner and outer air gap and their harmonics distribution are shown in Fig. 3. Sorting the harmonics by their amplitude, the dominant harmonics in both inner and outer air gap are the 2nd, 22nd, 24th and 46th components, which is the $(Z_s - Z_r)$ -th, Z_r -th, Z_s -th and $(Z_s + Z_r)$ -th order harmonic. Among these harmonic components in both air gaps, the 22nd component is produced by the rotor PM sources, the 24th component is produced by stator PM sources, the 2nd and 46th components are the harmonics excited by the modulation effect. Except the 46th component, other three dominant components are effective components which generates synchronous torque. This agrees with the principle discussed in the previous section. From Fig. 3(b), the amplitude ratio of each harmonic component, like the 22nd component and the 24th component, in the outer airgap

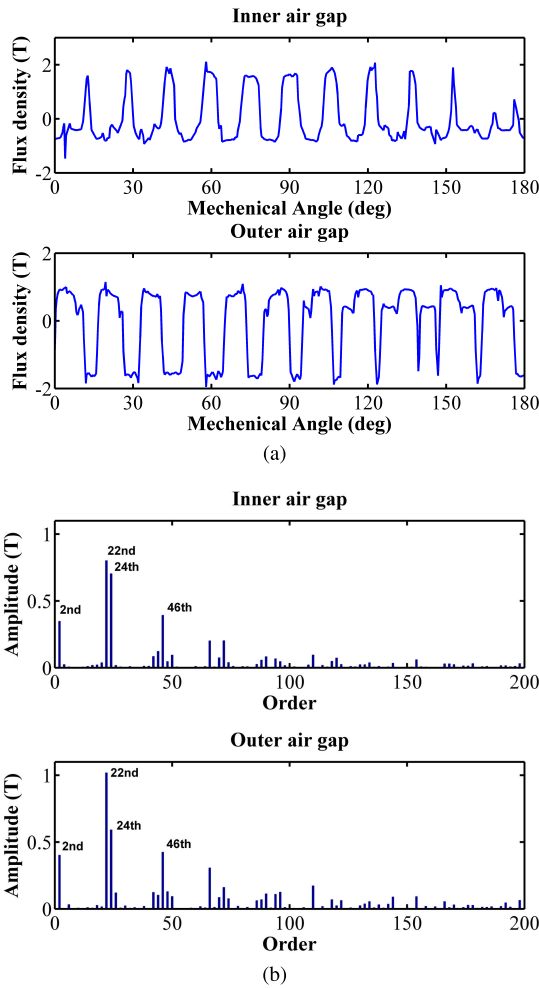


FIGURE 3. Flux density and harmonics distribution of inner and outer air gap at no load. (a) Flux density. (b) Harmonics distribution.

is quite different from the one of inner airgap. This is mainly because the volume ratio of stator PMs and rotor PMs is different for both inner and outer airgap, thus each harmonic component's amplitude varies.

The back EMF waveforms and their harmonics distribution at rated speed are given in Fig. 4. From Fig. 4(a), we can see that the three phases are symmetrical. Its harmonics distribution also shows that the EMF waveform is of good quality and close to sinusoidal. The fundamental component at the frequency of rated speed is much bigger than the rest of harmonics, as shown in Fig. 4(b).

B. FULL LOAD ANALYSIS

With the excitation of rated current, the current density is 3.9 A/mm². The magnetic flux density distribution can be calculated and the result is shown in Fig. 5. The result shows that the magnetic flux density distribution in stator and rotor is suitable, with the flux density less than 1.5 T in most area. The highest place of magnetic flux density appears in the yoke of the core and the teeth of stator. In both rotor cores, the flux density is relatively low.

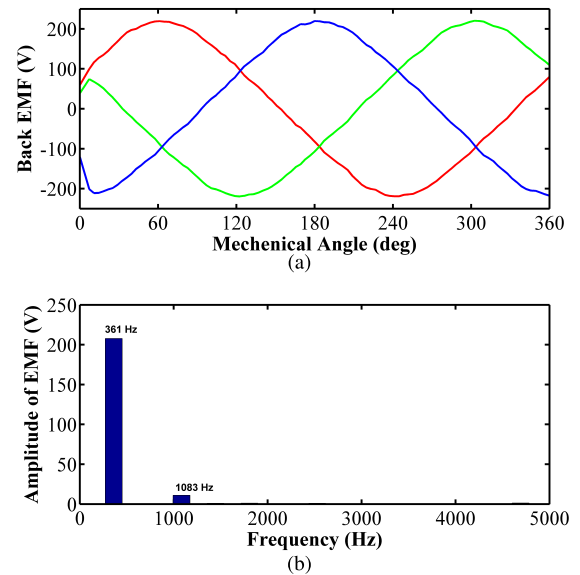


FIGURE 4. Back EMF waveform and harmonics distribution at no load. (a) Back EMF waveform. (b) Harmonics distribution.

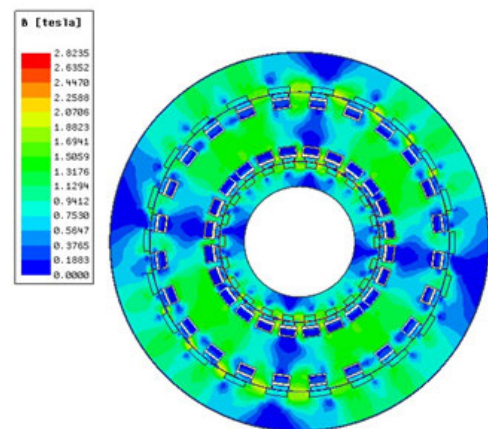


FIGURE 5. Magnetic flux density distribution at rated current.

The method of torque calculation is computing Maxwell stress tensor by FEM. The force applied to each element can be obtained by integrating the Maxwell stress tensor along the surface of the airgap. Thus, in 2D electromagnetic field FEM computation, the electromagnetic torque can be expressed as

$$T_{em} = \frac{L_{ef}}{\mu_0} \oint r^2 B_r B_\theta d\theta \tag{43}$$

where L_{ef} is the effective length of machine, r is the distance between each element in the airgap to the origin point of the machine, B_r and B_θ are the radial and tangential vectors of each element's magnetic flux density.

The electromagnetic torque can be calculated by FEM with (43) and plotted in Fig. 6, with the rated speed and current. From Fig. 6(a), the torque contribution of rotor PMs is 297 Nm, and the torque contribution of stator PMs

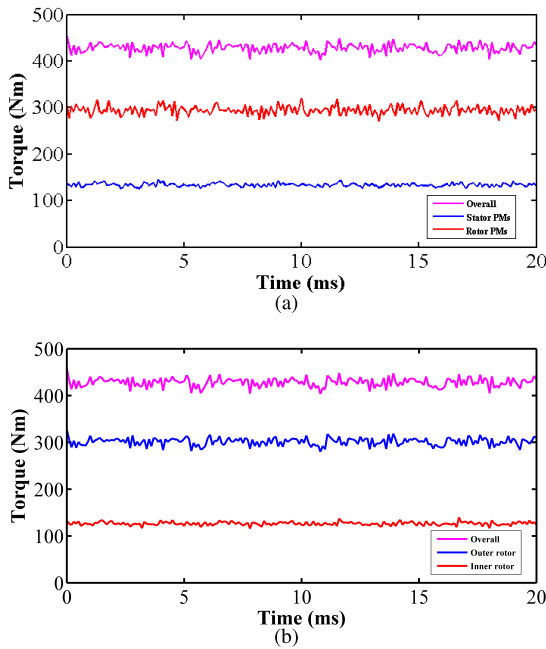


FIGURE 6. Rated torque waveform. (a) Torque contribution of stator PMs and rotor PMs. (b) Output torque of outer rotor and inner rotor.

is 134 Nm. It can be revealed that rotor PMs have better ability to generate torque than stator PMs.

The output torque of the inner rotor and outer rotor is 305 Nm and 125 Nm as shown in Fig. 6(b), respectively. It is clear that outer rotor generates more torque because of the larger peripheral dimension and PM size. The overall output torque is 430 Nm. The torque density per machine volume at the rated current is 36 kNm/m³.

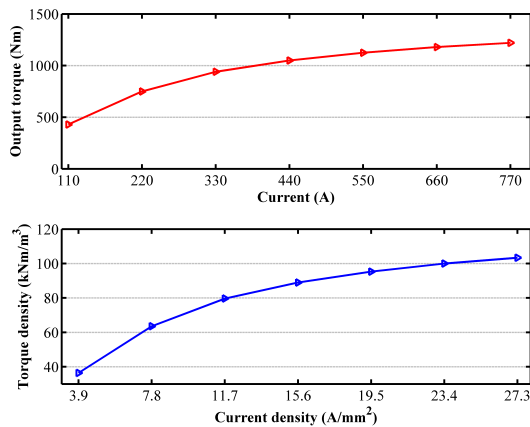


FIGURE 7. Torque-current and torque density per machine volume-current density curve.

The torque-current and torque density per machine volume-current density curve is shown in Fig. 7. The torque density per machine volume can reach 100 kNm/m³ with the proper cooling method when the current density reaches 25 A/mm², as shown in Fig. 7. The demagnetizing analysis

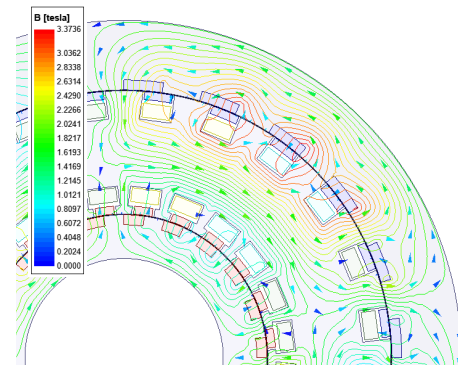


FIGURE 8. Flux density vector distribution when torque density per machine volume reaches 100 kNm/m³.

TABLE 5. Design data of different pole-pair configuration at rated current and rated speed.

Item	Proposed	Config. A	Config. B
Number of phases	3	3	3
Rated current (rms)	110 A	110 A	110 A
Rated speed	985 rpm	985 rpm	985 rpm
Rated torque	430 Nm	425Nm	370Nm
Number of stator slots	24	24	24
Outer diameter of stator	269 mm	269 mm	269 mm
Outer diameter of outer rotor	340 mm	340 mm	340 mm
Outer diameter of inner rotor	144 mm	144 mm	144 mm
Length of outer air gap	0.5 mm	0.5 mm	0.5 mm
Length of inner air gap	0.5 mm	0.5 mm	0.5 mm
Core length	130 mm	130 mm	130 mm
Slot depth	14 mm	14 mm	14 mm
Winding turns	4	4	4
PM number of stator	24*2	24*2	24*2
PM number of rotor	22*2	23*2	26*2
Pole-pair number of armature	2	1	2
Thickness of stator PMs	4 mm	4 mm	4 mm
Thickness of rotor PMs	5 mm	5 mm	5 mm
PM remanence	1.23 T	1.23 T	1.23 T
Torque ripple	40Nm	41Nm	49Nm
Copper loss	240W	240W	240W
Coreloss	2196W	5035W	3809W
Power factor	0.90	0.78	0.86
Efficiency	92%	87%	88%

at this state has been conducted. Comparing with the rated data, the flux density of PMs has about 5% slight drop. The flux density vector distribution at this state is shown in Fig. 8. From the direction of the vectors, it shows that the PMs have not reach the irreversible demagnetized operating point at this state.

C. COMPARISON ANALYSIS OF DIFFERENT SLOT/POLE CONFIGURATION

In order to find the best PM pole-pair number configuration, two other configurations are analyzed by FEM and compared with the proposed one. Except the difference in pole-pair number of rotor, all the other parameters are same. The results are shown in Table 5.

1) CONFIGURATION A

Configuration A is shown in Fig. 9. Its rotor pole-pair number is 23 and its stator pole-pair number is 24. The pole-pair number of the armature winding is set to be 1, according

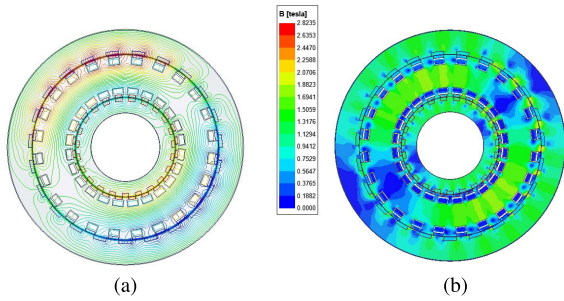


FIGURE 9. Magnetic distribution of Configuration A at rated current. (a) Magnetic flux line. (b) Magnetic flux density.

to (39). The gear ratio of rotor PM is 23, according to (42), which is higher than the proposed one of 11.

In principle, the output torque of Configuration A should be higher than the proposed one. However, because the magnetic field modulated is a one-pole-pair field, the flux density of the stator core is much higher than the proposed configuration, as shown in Fig. 9(b), which can reach 1.7 T in most area of the stator yoke. With the same stator yoke length as the proposed machine, the stator yoke is over saturated, which has greatly affected the torque generation and has increased the coreloss greatly as well. This makes this configuration inferior to the proposed one.

2) CONFIGURATION B

Configuration B has the rotor pole-pair number of 26 and the stator pole-pair number of 24, shown in Fig. 10. According to (40), the armature winding is as same as the proposed one, but its magnetic field has the opposite rotating direction with the proposed one. The gear ratio of rotor PM is 13, according to (42), which is slightly higher than the proposed one of 11 and the output torque should be also slightly higher.

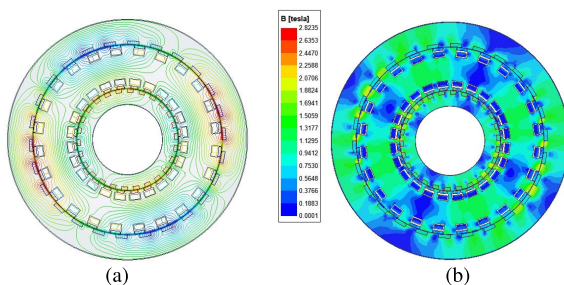


FIGURE 10. Magnetic distribution of Configuration B at rated current. (a) Magnetic flux line. (b) Magnetic flux density.

The reason why the output torque is lower is because the main harmonic components of magnetic flux density in the airgap of Configuration B which generate torque are the 2nd, 24th and 26th components. The amplitude of the 26th component is smaller than the 22nd component of proposed configuration because of the higher order. From Fig. 10(b), the flux density of Configuration B in stator core is also lower,

with the maximum of 1.2 T. Therefore, this configuration is also inferior to the proposed one.

D. COMPARISON ANALYSIS OF DIFFERENT STRUCTURE

To further prove the outstanding performance of the proposed machine, a normal dual-airgap permanent magnet Vernier machine (DAPMVM) based on [15] and a single-airgap dual permanent magnet Vernier machine (SADPMVM) are designed and compared with the proposed machine by using FEM. These two machines are designed to have the same peripheral dimension and winding configuration as the proposed machine. The detailed design data are shown in Table 6. The configuration and the magnetic flux at no load are shown in Fig. 11 and Fig. 12.

TABLE 6. Design data of different structures at rated current and rated speed.

Item	DADPMVM	DAPMVM	SADPMVM
Number of phases	3	3	3
Rated current (rms)	110 A	110 A	110 A
Rated speed	985 rpm	985 rpm	985 rpm
Rated torque	430 Nm	250 Nm	315 Nm
Torque density per machine volume	36 kNm/m ³	21 kNm/m ³	27 kNm/m ³
Number of stator slots	24	24	24
Outer diameter of stator	269 mm	269 mm	269 mm
Outer diameter of outer rotor	340 mm	340 mm	340 mm
Outer diameter of inner rotor	144 mm	144 mm	NA
Length of outer air gap	0.5 mm	0.5 mm	0.5 mm
Length of inner air gap	0.5 mm	0.5 mm	0.5 mm
Core length	130 mm	130 mm	130 mm
Slot depth	14 mm	14 mm	14 mm
Winding turns	4	4	4
PM number of stator	24*2	NA	24
PM number of inner rotor	22	22*2	NA
PM number of outer rotor	22	22*2	22
PM total volume	7.2×10 ⁻⁴ m ³	6.8×10 ⁻⁴ m ³	4.6×10 ⁻⁴ m ³
Torque density per PM usage	600 kNm/m ³	369 kNm/m ³	692 kNm/m ³
Thickness of stator PMs	4 mm	NA	4 mm
Thickness of rotor PMs	5 mm	4 mm	5 mm
PM remanence	1.23 T	1.23 T	1.23 T
Torque ripple	40Nm	35Nm	33Nm
Copper loss	240W	240W	240W
Coreloss	2196W	1419W	1416W
Power factor	0.90	0.90	0.90
Efficiency	92%	91%	93%

1) DUAL-AIRGAP PERMANENT MAGNET VERNIER MACHINE (DAPMVM)

This model is referred to [15], whose torque density per machine volume is 25 kNm/m³. In this paper, this model has been modified to have the same overall size as the proposed machine. DAPMVM also has the structure of concentric inner and outer rotor. The difference from the proposed machine is that the PM sources of DAPMVM are all equipped on the rotor side. Every two face-to-face PMs on inner rotor and outer rotor should also have the opposite radial magnetization direction, in order to make the flux flowing towards the stator yoke. Two adjacent PMs have the opposite radial direction of magnetization and form a magnetic pole pair, as the conventional machines.

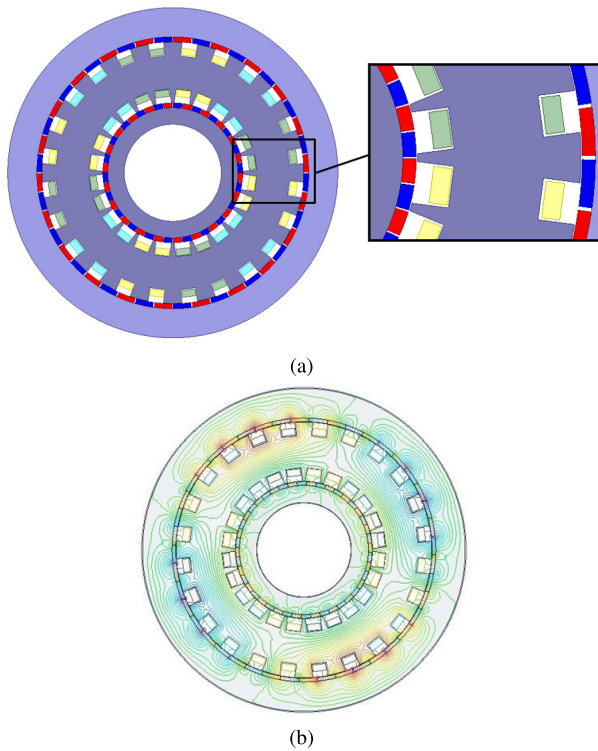


FIGURE 11. Dual-airgap permanent magnet Vernier Machine. (a) Configuration. (b) Magnetic flux distribution at no load.

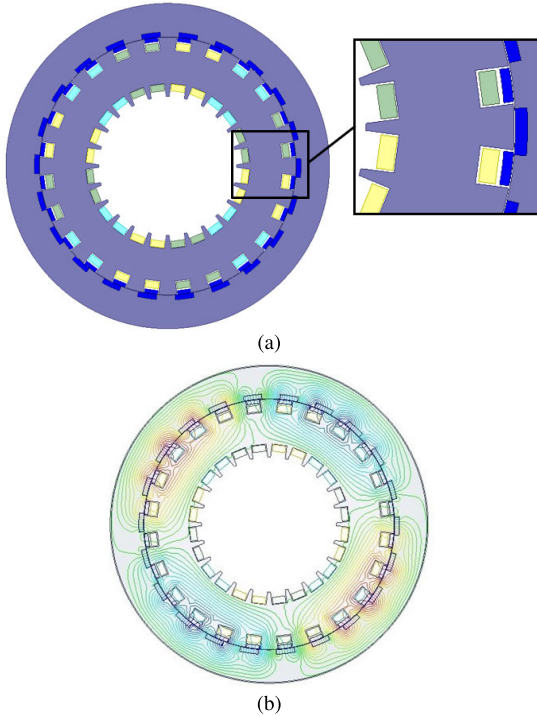


FIGURE 12. Single-airgap dual permanent magnet Vernier Machine. (a) Configuration. (b) Magnetic flux distribution at no load.

From Table 6, with the same winding and rated current input, the output torque of DAPMVM is smaller than the output torque of DADPMVM. The main reason is that the

adjacent material of the DAPMVM’s PMs in tangential direction is also permanent magnet, which is different from the ferromagnetic material of DADPMVM’s core tooth. The permeability of magnetic substance is almost equal to vacuum, which is much lower than the permeability of steel, thus makes the magnetic resistance in the magnetic loop much higher. Another reason is the magnetic flux leakage caused by the opposite magnetization direction of adjacent PM source. These are also the reasons that the core loss of DAPMVM is smaller than DADPMVM, as Table 6 shows, for the average flux density of DAPMVM is lower than the proposed machine. This makes DAPMVM to have inferior performance than the proposed machine.

2) SINGLE-AIRGAP DUAL PERMANENT MAGNET VERNIER MACHINE (SADPMVM)

For SADPMVM, it has the same dual airgap structure as the proposed machine. Except there is no inner rotor and no PM sources are mounted on the inner side of the stator, other configurations and peripheral dimensions are exactly the same.

From Table 6, the rated output of SADPMVM can be found slightly higher than the output of the DADPMVM’s outer rotor. This is mainly because for DADPMVM, the inner air gap’s flux has crowded out certain outer air gap flux, which leads to a small drop in outer rotor’s torque.

Although SADPMVM’s torque density per PM usage is slightly higher than the proposed one, and it uses the drum winding which is the same as the proposed machine, only the outer side of the winding is used to excite its outer rotor. The size of machine is not fully used. From Table 6, it is clear that the overall output torque and the torque density per machine volume are lower when comparing with the design of dual rotor. The core loss of SADPMVM is the smallest among three designs.

IV. CONCLUSION

A novel DADPMVM is designed and analyzed by using FEM in this paper. By combining the dual-airgap structure and dual PM structure, the torque density can be greatly improved within the limited machine volume. The proposed machine’s performance at rated current has been compared with two different slot/pole configurations and two different structures designed in the same peripheral dimension. The result of the comparison has proved the outstanding performance of DADPMVM.

The proposed DADPMVM have the following merits:

- 1) The dual PM configuration enables the stator and the rotor to modulate the utility harmonic components in both air gaps synchronously. This contributes to the synchronous high back EMF generation and synchronous high torque generation, which makes the proposed machine to have high torque density.
- 2) The dual-airgap structure enables the limited volume of the machine to be fully utilized. The additional airgap

and the inner rotor have contributed additional torque, thus makes the torque density per machine volume further increased.

- 3) With the use of drum winding, the excitation of two rotors can be induced with only one set of coil. Consequently, the structure can be further simplified. When comparing with the conventional windings, end winding length of the drum winding is much shorter, hence the copper losses are further reduced.

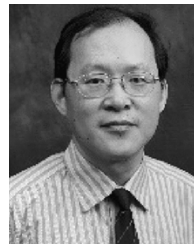
Comparing with normal PMVM, the proposed DADP-MVM has higher torque density per machine volume, higher use of winding length and lower copper losses. The torque density can exceed 100 kNm/ m³ when proper cooling method is used.

REFERENCES

- [1] D. Li, R. Qu, and T. A. Lipo, "High-power-factor Vernier permanent-magnet machines," *IEEE Trans. Ind. Appl.*, vol. 50, no. 6, pp. 3664–3674, Nov. 2014.
- [2] A. Ishizaki, "Theory and optimum design of PM Vernier motor," in *Proc. 7th Int. Conf. Electr. Mach. Drives*, Durham, U.K., Sep. 1995, pp. 208–212.
- [3] X. Zhao, S. Niu, and W. Fu, "Design of a novel parallel-hybrid-excited dual-PM machine based on armature harmonics diversity for electric vehicle propulsion," *IEEE Trans. Ind. Electron.*, vol. 66, no. 6, pp. 4209–4219, Jun. 2019.
- [4] H. Yang, H. Lin, Z. Q. Zhu, S. Lyu, and K. Wang, "A novel dual-sided PM variable flux memory machine," *IEEE Trans. Magn.*, vol. 54, no. 11, Nov. 2018, Art. no. 8110605.
- [5] B. Kim and T. A. Lipo, "Analysis of a PM Vernier motor with spoke structure," *IEEE Trans. Ind. Appl.*, vol. 52, no. 1, pp. 217–225, Jan. 2016.
- [6] K. Atallah and D. Howe, "A novel high-performance magnetic gear," *IEEE Trans. Magn.*, vol. 37, no. 4, pp. 2844–2846, Jul. 2001.
- [7] A. Toba and T. A. Lipo, "Generic torque-maximizing design methodology of surface permanent-magnet Vernier machine," *IEEE Trans. Ind. Appl.*, vol. 36, no. 6, pp. 1539–1546, Nov./Dec. 2000.
- [8] Y. Chen, W. Fu, and X. Weng, "A concept of general flux-modulated electric machines based on a unified theory and its application to developing a novel doubly-fed dual-stator motor," *IEEE Trans. Ind. Electron.*, vol. 64, no. 12, pp. 9914–9923, Dec. 2017.
- [9] Q. Wang, S. Niu, and L. Yang, "Design optimization and comparative study of novel dual-PM excited machines," *IEEE Trans. Ind. Electron.*, vol. 64, no. 12, pp. 9924–9933, Dec. 2017.
- [10] M. Lin, D. Li, K. Xie, X. Han, X. Ren, and R. Qu, "Comparison between pole-changing and dual-stator line-start permanent magnet Vernier machine," *IEEE Trans. Ind. Appl.*, vol. 56, no. 4, pp. 3700–3709, Aug. 2020.
- [11] X. Zhao, S. Niu, and W. Fu, "Torque component quantification and design guideline for dual permanent magnet Vernier machine," *IEEE Trans. Magn.*, vol. 55, no. 6, Jun. 2019, Art. no. 8101905.
- [12] Q. Lin, S. Niu, and W. N. Fu, "Design and optimization of a dual-permanent-magnet Vernier machine with a novel optimization model," *IEEE Trans. Magn.*, vol. 56, no. 3, Mar. 2020, Art. no. 7512705.
- [13] Y. Tasaki, R. Hosoya, Y. Kashitani, and S. Shimomura, "Design of the Vernier machine with permanent magnets on both stator and rotor side," in *Proc. 7th Int. Power Electron. Motion Control Conf.*, Harbin, China, Jun. 2012, pp. 302–309.
- [14] S. Niu, K. T. Chau, and C. Yu, "Quantitative comparison of double-stator and traditional permanent magnet brushless machines," *J. Appl. Phys.*, vol. 105, no. 7, Feb. 2009, Art. no. 07F105.
- [15] S. Niu, S. L. Ho, W. N. Fu, and L. L. Wang, "Quantitative comparison of novel Vernier permanent magnet machines," *IEEE Trans. Magn.*, vol. 46, no. 6, pp. 2032–2035, Jun. 2010.
- [16] A. Toba and T. A. Lipo, "Novel dual-excitation permanent magnet Vernier machine," in *Proc. IEEE Ind. Appl. Soc. Annu. Meeting (IAS)*, vol. 4, Oct. 1999, pp. 2539–2544.



MINGYUAN JIANG received the B.Eng. degree in electrical engineering and automation from Shanghai Maritime University, Shanghai, China, in 2020. He is currently pursuing the M.Sc. degree in electrical engineering with The Hong Kong Polytechnic University, Hong Kong, SAR, China. His main research interests include design, analysis, and optimization of electric machine.



WEINONG FU received the B.Eng. degree from the Hefei University of Technology, Hefei, China, in 1982, the M.Eng. degree from the Shanghai University of Technology, Shanghai, China, in 1989, and the Ph.D. degree from The Hong Kong Polytechnic University, Hong Kong, in 1999, all in electrical engineering. In 2007, he was one of the key developers with Ansoft Corporation, Pittsburgh, PA, USA. He has about seven years of working experience with Ansoft, focusing on the development of the commercial software Maxwell. He is currently a Professor with The Hong Kong Polytechnic University. He has authored or coauthored more than 240 articles in refereed journals. His current research interests include numerical methods of electromagnetic field computation, optimal design of electric devices based on numerical models, applied electromagnetics, and novel electric machines.



SHUANGXIA NIU (Senior Member, IEEE) received the B.Sc. and M.Sc. degrees in electrical engineering from the School of Electrical Engineering and Automation, Tianjin University, Tianjin, China, and the Ph.D. degree in electrical engineering from the Department of Electrical and Electronic Engineering, The University of Hong Kong, Hong Kong. Since 2009, she has been with The Hong Kong Polytechnic University, Hong Kong, where she is currently an Associate Professor with the Department of Electrical Engineering. She has authored or coauthored more than 100 articles in leading journals. Her research interests include novel electrical machines and drives, renewable energy conversion systems, and applied electromagnetics.

...